

THE REST-FRAME EXTREME ULTRAVIOLET SPECTRAL PROPERTIES OF QSOs

RANDAL C. TELFER¹, WEI ZHENG¹, GERARD A. KRISS^{1,2}, AND ARTHUR F. DAVIDSEN¹
Accepted for publication in February 1 edition of the Astrophysical Journal

ABSTRACT

We use a sample of 332 Hubble Space Telescope spectra of 184 QSOs with $z > 0.33$ to study the typical ultraviolet spectral properties of QSOs, with emphasis on the ionizing continuum. Our sample is nearly twice as large as that of Zheng et al. (1997) and provides much better spectral coverage in the extreme ultraviolet (EUV). The overall composite continuum can be described by a power law with index $\alpha_{EUV} = -1.76 \pm 0.12$ ($f_\nu \propto \nu^\alpha$) between 500 and 1200 Å. The corresponding results for subsamples of radio-quiet and radio-loud QSOs are $\alpha_{EUV} = -1.57 \pm 0.17$ and $\alpha_{EUV} = -1.96 \pm 0.12$, respectively. We also derive α_{EUV} for as many individual objects in our sample as possible, totaling 39 radio-quiet and 40 radio-loud QSOs. The typical individually measured values of α_{EUV} are in good agreement with the composites. We find no evidence for evolution of α_{EUV} with redshift for either radio-loud or radio-quiet QSOs. However, we do find marginal evidence for a trend towards harder EUV spectra with increasing luminosity for radio-loud objects. An extrapolation of our radio-quiet QSO spectrum is consistent with existing X-ray data, suggesting that the ionizing continuum may be represented by a single power law. The resulting spectrum is roughly in agreement with models of the intergalactic medium photoionized by the integrated radiation from QSOs.

Subject headings: ultraviolet: galaxies — quasars: general — quasars: emission lines

1. INTRODUCTION

One of the most striking characteristics of QSO spectra is their similarity, even over a span of a few decades in luminosity and a large range in redshift. This similarity in spectral properties makes the production of composite spectra an appealing and useful tool for studying the general properties of the QSO population. In recent years, the number of known quasars has increased dramatically due to comprehensive surveys and, in particular, the effective use of fiber-optic spectrographs. Very high signal-to-noise ratio (S/N) composites consisting of hundreds to thousands of optical spectra have been created out of spectral data acquired for various surveys, including composites from the Large Bright Quasar Survey (LBQS; Francis et al. 1991), the FIRST survey (Brotherton et al. 2001), and the Sloan Digital Sky Survey (SDSS; Vanden Berk et al. 2001). Composites of subgroups of QSOs have also been generated to study the dependence of the spectra on particular properties, such as radio brightness (Francis, Hooper, & Impey 1993; Brotherton et al. 2001), X-ray brightness (Green 1998), and radio morphology (Baker & Hunstead 1995). The ultimately enormous number of QSO spectra from the SDSS promises the ability to study in detail the spectral dependence on various properties, including luminosity and redshift.

These studies have contributed greatly to our detailed knowledge of QSO spectral properties at wavelengths longer than Ly α . However, studies performed with optical spectra are limited in the amount of information they can supply at wavelengths shorter than Ly α . These objects can only be observed below Ly α for $z \gtrsim 2$ from the ground, and in practice the limit from survey spectra is even more restrictive. For example, the SDSS spectroscopic data begin at ~ 4000 Å, and thus Ly α can only be observed for $z > 2.3$. At such high redshift, the Ly α forest absorption is extremely dense, depressing the flux and greatly reducing the S/N. Exploring the spectral properties of

QSOs below Ly α and deeper into the extreme ultraviolet (EUV) thus requires the use of ultraviolet spectra.

The EUV range is important for several reasons: (1) The photons below 912 Å are believed to be the main sources of line formation via photoionization and they should be related to the emission lines seen in the near ultraviolet (NUV) and optical regions; (2) The continuum shape in this range helps define the peak in the QSO energy output in the UV known as the Big Blue Bump, which may be relevant to the soft X-ray fluxes. Evidence suggests that the EUV continuum is related to the soft X-ray, which may help to explain the origin of the Big Blue Bump; (3) EUV emission from QSOs is thought to be an important, if not dominant, source of ionization for the intergalactic medium (IGM), and the physical state of the IGM can depend on the exact shape of the ionizing continuum.

The optical composites suggest that the continuum can be represented by a power law between ~ 1200 and 5000 Å, with a power-law index α around -0.3 to -0.5 ($F_\nu \propto \nu^\alpha$). However, Zheng et al. (1997, hereafter Z97) find that there is a distinct change in the spectral shape in the EUV. Using the Hubble Space Telescope (HST) Faint Object Spectrograph (FOS) spectra of 101 quasars with $z > 0.33$, Z97 produced a composite spectrum that covers a range between 350 and 3000 Å. The resulting composite indicated a break in the continuum shape around 1050 Å. The EUV continuum shape for the Z97 radio-quiet composite could be approximated with a power law of index -1.8 . By comparison, Laor et al. (1997a) derived a mean soft X-ray power-law index of -1.72 for a sample of $z < 0.4$ radio-quiet QSOs. The similarity of the power-law indices in these two independent studies suggests a common origin for the UV / X-ray continuum. Thus, although the full ionizing continuum of QSOs is not directly observable due to the opacity of the Galaxy, by studying a significant portion of the EUV continuum we may plausibly gain knowledge of the ionizing

¹ Center for Astrophysical Sciences, Johns Hopkins University, Baltimore, MD, 21218-2686² Space Telescope Science Institute, 3700 San Martin Drive, Baltimore, MD, 21218

spectrum as a whole.

In this paper, we extend the work of Z97 to include the full sample of $z > 0.33$ QSO observations with the HST FOS and Goddard High Resolution Spectrograph (GHRS), as well as available Space Telescope Imaging Spectrograph (STIS) data. We begin in §2 by describing the sample, our selection criteria, and the details of our processing of the data. We proceed in §3 by describing the technique for creating our composites. In §4 we first discuss our results and the corresponding uncertainties. We then discuss how we estimate luminosities using the composite for the purpose of characterizing the sample. This is followed by a presentation of our radio-loud and radio-quiet composites, and finally a discussion of the broad emission-line properties. In §5 we discuss how we characterize the continuum of individual objects in our sample. We compare the results with the composite and also search for possible correlations of the EUV continuum with luminosity and redshift. We compare our results with other composites in §6, and then discuss the implications of our results. We summarize our results in §7.

2. DATA

2.1. The Sample

Our data sample consists of all known spectra of $z > 0.33$ QSOs taken with the HST FOS and GHRS. We add to this all QSO spectra from STIS that were publicly available as of 2000 August. The redshift limit was chosen such that the region below the intrinsic Lyman limit (912 Å) is observable by HST. We removed spectra from the sample for the following reasons:

1. The object is a known or suspected Broad Absorption Line QSO.
2. The spectrum is high resolution with small wavelength coverage (medium and high resolution modes on GHRS and STIS).
3. The S/N is very low ($\lesssim 1$ per pixel).
4. After trimming (see §2.2), very little spectrum remains ($\Delta\lambda/\lambda \lesssim 0.2$).

In addition, if two spectra are almost entirely redundant – for example, if both FOS G130H and GHRS G140L data are available – then only the higher quality data are used. However, in cases where there is only a partial redundancy (for example, FOS G270H and FOS G160L), both spectra are included.

After applying these selection criteria, our final sample consists of 332 spectra of 184 QSOs, nearly twice as large as the sample from Z97³. This final sample contains 13 spectra with FOS grating G130H, 93 with FOS G190H, 139 with FOS G270H, 25 with FOS G400H, 2 with FOS G570H, 51 with FOS G160L, 6 with GHRS G140L, 2 with STIS G140L, and 1 with STIS G230L. The redshift distribution of the corresponding QSOs is shown in Figure 1, along with the corresponding distribution of Z97.

³ Z97 stated that their sample consisted of 284 spectra of 101 QSOs. However, many of these spectra were separate observations of the same QSO using the same instrument and grating that we have since combined. Counting spectra in a manner consistent with the present sample, the Z97 sample consisted of 184 spectra of 101 QSOs.

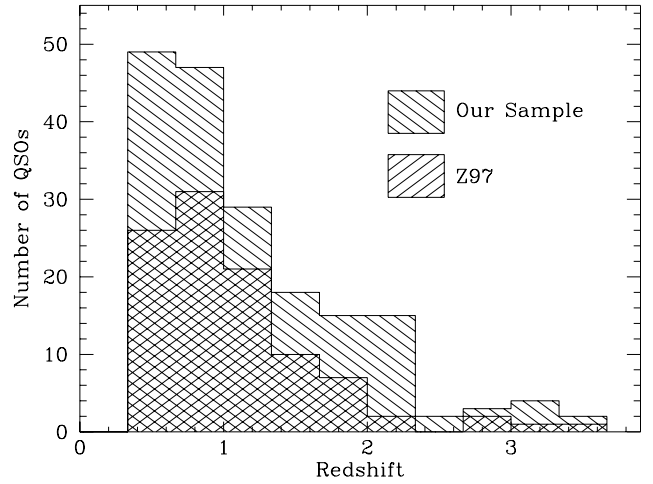


FIG. 1.— Redshift distribution of sample QSOs with a bin size of 0.33, comparing the current sample with Z97.

2.2. Reduction

Prior to combination, each spectrum is processed with a series of tasks which we describe in more detail below. Specifically:

1. The spectrum is corrected for Galactic extinction.
2. Strong features not intrinsic to the QSO are masked out, including instrumental artifacts, airglow, and strong absorption.
3. If there are one or more intervening Lyman limit absorbers in the sight line for which the optical depth can be well determined and the data below the Lyman limits meet our S/N criterion (S/N per pixel $\gtrsim 1$), we correct for the Lyman continuum absorption of the systems.
4. If there is an optically thick Lyman limit absorber in the spectrum such that the data below the Lyman edge are not recoverable, we remove the data below the edge from the spectrum.
5. A statistical correction is applied for the accumulated Lyman line and Lyman limit opacity of absorbers below our detection threshold.
6. The spectrum is shifted into the object rest frame.
7. The spectrum is resampled into common wavelength bins to facilitate the combination process.

The order in which these steps are applied is unimportant, with the exceptions that the Galactic extinction correction must be performed before the spectra are shifted into the rest frame and the resampling must be performed after the spectra are shifted. We now discuss the individual steps in appropriate detail.

The Galactic extinction correction is performed according to the analytic form of Cardelli, Clayton, & Mathis (1988) using $E(B-V)$ values from Schlegel, Finkbeiner, & Davis (1998). We assume $R_V = 3.1$ for all objects.

We mask undesired data by simply flagging the individual pixels involved so that they are ignored by the code that combines the spectra. Some spectra contain odd spikes that are clearly not intrinsic to the QSO, probably caused by malfunctioning diodes not recognized by the calibration software. These are masked out, as are airglow lines from Ly α and O I $\lambda 1304$ in FOS G130H, FOS G160L, and GHRS G140L spectra. Also, all FOS G160L data above 2300 Å are removed as this region is generally contaminated by second-order Ly α airglow. We search each spectrum by eye for strong absorption features that change the apparent character of the spectrum and could have some influence on the final composite, including damped lines and strong clusters of lines.

For two well-studied objects, LB 9612 and HS 1700+641, we correct for the Lyman limit absorbers using redshifts and column densities from the literature, Dinshaw et al. (1998) and Vogel & Reimers (1995), respectively. For all other objects, the individual Lyman limit systems are identified by eye. For most systems the redshift is well-determined by the identification of many Lyman lines, although in the low-resolution FOS 160L data this is generally not possible and the redshift of the system is estimated from the position of the Lyman break itself. The optical depth of each Lyman limit is estimated as $\ln(F_+/F_-)$, where F_- is the median flux of the pixels just below the break, from 890–911 Å in the absorber frame, and F_+ is the median flux of the pixels in the windows 933–936, 940–948, and 952–960 Å in the absorber frame. These windows are chosen to avoid absorption by the Lyman lines. After the correction for the Lyman limit is performed, typically a large absorption feature remains due to the clustering of high-order Lyman lines that is masked out as described above. If we cannot achieve an acceptable correction because the S/N below the break is too low, which generally occurs for $\tau \gtrsim 2$, the portion below the break is simply removed.

We are confident that we are correcting for nearly all Lyman limit absorbers with $\tau > 0.3$, corresponding to a neutral hydrogen column density $\log N(\text{HI})(\text{cm}^{-2}) > 16.7$. However, the accumulated absorption of weaker absorbers, being much more numerous, contributes strongly to the opacity of high-redshift objects, producing a broad trough centered near 700 Å known as the Lyman valley (Møller & Jakobsen 1990). We therefore apply a statistical correction for these unidentified absorbers.

We characterize the distribution of Lyman forest absorbers by the empirical formula:

$$\frac{\partial^2 n}{\partial z \partial N} \propto (1+z)^\gamma N^{-\beta}, \quad (1)$$

where n is the number of lines, z is redshift, and N is the column density of neutral hydrogen. As first pointed out by Tytler (1987), $\beta = 1.5$ provides a reasonable fit to the column density distribution of Lyman forest absorbers over the entire range of observable column densities ($\sim 3 \times 10^{12} - 10^{22} \text{ cm}^{-2}$). However, known deviations from a pure power law are large enough to have observable consequences on the Lyman valley correction. We adopt values from Petitjean et al. (1993): $\beta = 1.83$ for $3 \times 10^{14} < N < 10^{16} \text{ cm}^{-2}$ and $\beta = 1.32$ for $N > 10^{16} \text{ cm}^{-2}$. For $N < 3 \times 10^{14} \text{ cm}^{-2}$, we use $\beta = 1.46$ from Hu et al. (1995), down to their limiting column density of $3 \times 10^{12} \text{ cm}^{-2}$. For the redshift evolution power-law index, we use $\gamma = 2.46$ (Press, Rybicki, & Schneider 1993). The entire distribution is normalized by demanding that the line number be consistent with Hu et al. (1995) at the low column density end. Specifically, we set $\partial^2 n / \partial z \partial N = 6.76 \times 10^{-13}$ at $z = 2.8$ and $N = 10^{14} \text{ cm}^{-2}$. At

breaks in the index β , we demand that the distribution be continuous. For calculating the line opacity, we assume a b parameter of 30 km s^{-1} .

When the wavelengths are divided by $(1+z)$ to shift the spectra into the object rest frame, the fluxes in F_λ are multiplied by $(1+z)$. Each resulting spectrum then has the property that when the flux is multiplied by $4\pi D_L^2$, where D_L is the luminosity distance to the QSO, the result is the true luminosity L_λ of the QSO.

The spectra are resampled into aligned wavelength bins of common size. The flux in each of the bins of a resampled spectrum is determined as the mean of the flux in the bins of the old spectrum that overlap the new bin weighted by the extent of the overlap between the new bin and old bin in wavelength space. The errors per rebinned pixel are calculated in a manner consistent with this weighting. More precisely, we use the following formulas for calculating the rebinned fluxes and errors:

$$F_r = \frac{\sum_i F_i \delta \lambda'_i}{\sum_i \delta \lambda'_i} \quad (2)$$

$$E_r = \frac{\{\sum_i [(E_i \delta \lambda'_i)^2 (\delta \lambda_i / \delta \lambda'_i)]\}^{1/2}}{\sum_i \delta \lambda'_i}, \quad (3)$$

where F_r and E_r are respectively the flux and error of the rebinned pixel, F_i and E_i are the fluxes and errors in the pixels of the original spectrum, $\delta \lambda_i$ are the sizes of the original bins, and $\delta \lambda'_i$ are the overlap of the old pixels with the new bin. The term $\delta \lambda_i / \delta \lambda'_i$ in the error corrects for the fact that the error in the flux for a fraction of a pixel scales as the $-1/2$ power of the overlap. This method introduces correlated errors between adjacent pixels, but we do not track the covariant errors.

3. COMBINATION TECHNIQUE

The usual method of producing composite spectra is the bootstrap. In the bootstrap method, the spectra are included in sorted order, either from shorter wavelength coverage to longer or vice versa. The composite is then constructed as follows:

1. The first spectrum is defined to be the partially formed composite, perhaps with some arbitrary renormalization for convenience.
2. The next spectrum is renormalized such that the mean flux of the spectrum and the partially formed composite are the same in the region over which the two overlap, excluding regions of strong emission lines.
3. A new composite is computed, this being the mean flux in each wavelength bin of the contributing spectra.
4. Steps 2 and 3 are repeated until all spectra are included.

The primary source of flexibility in this method is the manner in which the spectra are normalized. For the normalization routine, we mask out wavelength regions with strong emission lines; specifically, 750–800, 1000–1050, 1160–1265, 1380–1420, 1470–1610, 1830–1950, and 2700–2880 Å. The normalization of the spectra will therefore be driven by the continuum, which is our primary interest. In calculating the normalization factor for each spectrum, each pixel is weighted by the number of spectra contributing to the partially formed composite. This prevents the normalization from being dominated by regions of the composite that are determined by few objects and

are therefore uncertain. Thus, each spectrum is renormalized by multiplying the flux at each pixel by a factor

$$f_{\text{renorm}} = \frac{\sum_i F_{c,i} N_{c,i}}{\sum_i F_{s,i} N_{c,i}}, \quad (4)$$

where F_c is the flux in the partially formed composite, N_c is the number of spectra contributing to the composite, and F_s is the flux in the spectrum to be renormalized. The sum is over the wavelength region where the two overlap, excluding the masked wavelength regions.

The bootstrap method has a potential drawback in that it can be sensitive to the order in which spectra are added to the composite (longer wavelengths to shorter or vice versa), particularly at the beginning of the process where only a few spectra, which may not be representative of the entire sample, are determining the shape of the composite. To avoid this, we use a variation on the bootstrap method. As is evident in Figure 2, which shows the number of spectra in our sample as a function of wavelength, the number of spectra reaches a maximum in the region around Ly α . We therefore use the spectra in this middle region to define well the central portion of the composite, then bootstrap to the extremes. We choose the region from 1050–1150 Å as the central window, since it is relatively free of emission lines. We divide the overall sample into three subsamples: (1) the spectra that include the entire central spectral window, (2) those at longer wavelengths, and (3) those at shorter wavelengths. In our method, we first create a composite of just the spectra in group (1), where we renormalize each spectrum so that the mean flux in the central window is unity. Those in group (2) are then bootstrapped in sorted order to longer wavelengths as described before, then group (3) is bootstrapped to the shortest wavelengths. Since the central region is well defined by group (1), the order in which group (2) and group (3) are included is unimportant.

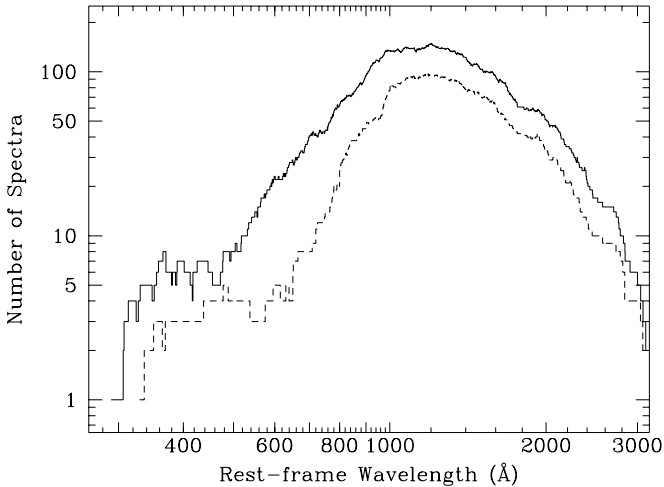


FIG. 2.— Number of merging spectra in the overall composite as a function of wavelength (solid line). The corresponding plot for Z97 (dashed line) is shown for comparison.

4. RESULTS

4.1. Overall Composite

The number of spectra contributing to this composite as a function of wavelength is shown in Figure 2, and the S/N per 230 km s $^{-1}$ is shown in Figure 3. The final overall composite is shown in Figure 4 with some of the strong emission lines

marked. The S/N is computed per 230 km s $^{-1}$ since this roughly represents the resolution of the FOS when used with the high-resolution gratings. The spikes in the S/N at the lowest wavelengths are real, and reflect very high S/N data obtained to study the He II Gunn-Peterson effect.

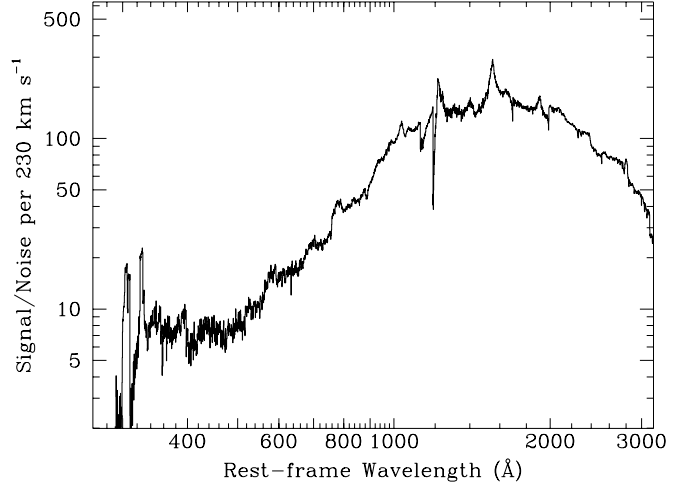


FIG. 3.— Signal-to-noise ratio in the overall composite per bin of 230 km s $^{-1}$, approximately the resolution of the FOS with the high-resolution gratings.

The composite clearly shows the break in the power-law index near Ly α as reported by Z97, as do the subset composites that we discuss later. Therefore, to characterize the continuum, we fit the composite with a broken power law using the IRAF task *specfit* (Kriss 1994), selecting wavelength windows free of emission lines for the fitting. Specifically, the wavelength windows we use are 350–750, 800–820, 850–900, 1095–1110, 1135–1150, 1450–1470, 1975–2010, and 2150–2200 Å. The exact location of the break is not well determined due to the high density of emission lines in the region of the break. For our fits the break wavelength varies from around 1200 to 1300 Å, depending on the particular subset. Throughout this paper, we will refer to the power-law index longward of the break as α_{NUV} and that shortward of the break as α_{EUV} , where both indices are defined by $f_\nu \propto \nu^\alpha$.

The composite deviates from a broken power law with a slight hardening of the spectrum shortward of 500 Å. As can be seen in Figure 2, below 500 Å fewer than ten spectra are contributing at any given wavelength. The fact that only a few spectra are contributing in this region is enough to raise doubt as to whether this portion of the composite is representative of all QSOs. Equally notable, however, is the significant flattening in the distribution of the number of spectra with wavelength below 500 Å. Above 500 Å, the shape of the distribution of the number of spectra with wavelength is roughly what one would expect from a random sampling of spectra of QSOs at various redshifts. The flattening below 500 Å is indicative of the strong bias towards observing those few QSOs that are bright enough in this region to obtain spectra with the HST, objects with preferentially hard UV spectra. We believe that the composite shape below 500 Å is likely not representative of the overall population of QSOs. Therefore, in addition to the fit with the windows stated above, we also produce a fit excluding the region below 500 Å.

There are several possible choices as to the error array to use

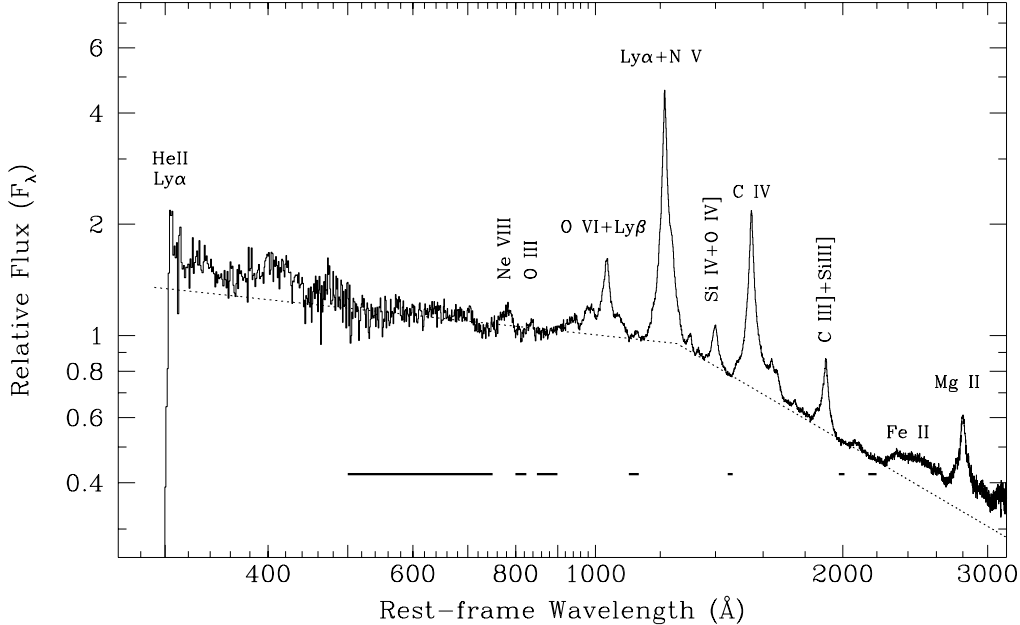


FIG. 4.— Overall mean composite QSO spectrum in 1 Å bins with some prominent emission lines marked. The dotted line shows the best fit broken power-law continuum, excluding the region below 500 Å. The lines at the bottom indicate the continuum windows used in the fit.

in computing χ^2 for the fitting process. We considered using the propagated error array of the composite, reflected in Figure 3. However, this has the undesirable result of giving too little weight to the shorter wavelengths ($\lesssim 800$ Å), both because many fewer objects contribute at these wavelengths and because the contributing spectra are generally of fainter, high-redshift objects and therefore have inherently lower S/N. We attempted using equal weighting for all pixels, but this only reverses the problem; the fits are driven strongly by the most extreme wavelengths. The RMS deviation of the spectral fluxes is another possible choice, but due to the fairly small number of objects contributing at the shortest wavelengths, this turns out to produce unreliable results. The main problem is that χ^2 is often dominated by regions where there are only a few spectra contributing that happen to have similar spectral shapes, resulting in a low value for the RMS deviation. Our solution is to use an error array that consists of the flux of the composite, smoothed by 10 Å to eliminate pixel-to-pixel noise, and divided by the square root of the number of contributing spectra. The result is to give a weighting to each pixel in the fit that scales linearly as the number of contributing spectra. A different way of viewing this solution is that the resulting errors are proportional to what would result from using the propagated error array if the S/N of all the individual spectra were equal, thus eliminating the bias towards high S/N spectra. We find that with this method we consistently obtain fits that characterize the spectrum well. The best-fit indices, as well as some information about the sample, are shown as the first line in Table 1. The quantity $\langle z \rangle$ is the mean redshift of the objects in the sample, and $\langle L \rangle$ is the mean value of $\log \lambda L_\lambda$ at 1100 Å for the sample objects in units of erg s⁻¹, calculated as described in §4.3. The best fit excluding the region below 500 Å is shown as the dotted line in Figure 4, and the continuum windows used in the fit are shown below the composite.

4.2. Uncertainties

Because of the high S/N of the composite, the formal errors on the measured power-law indices from the fits are negligibly small. The uncertainties are thus dominated by the uncertainty associated with producing a composite from our particular sample, as well as the flux corrections that we apply. We now discuss a few of these sources of uncertainty in detail.

The dominant uncertainty is that associated with our particular set of sample spectra, since the scatter in spectral shapes for individual objects is quite large (see §5). To estimate the resulting uncertainty on the parameterization of the continuum, we implement the bootstrap resampling technique. Given the 332 spectra in the complete sample, we create 1000 random samplings of these 332 spectra with replacement, fitting each one as we did the true composite. The results are distributions in the measured values of the power-law indices, and we calculate the 1 σ errors in the indices from these distributions.

To investigate the degree to which our results depend on the Galactic extinction correction, we repeated the analysis both with no extinction and with $E(B-V)$ doubled for each object. We find that the EUV continuum is insensitive to these changes, as shown in Figure 5. The reason for this at first surprising result is that since there are very few FOS G130H spectra in the sample, the EUV portion of the composite is produced dominantly by G190H spectra. The G190H bandpass contains the 2200 Å bump in the Galactic extinction curve, and as a result, the shape of the extinction curve is not monotonic. The extinction correction for a G190H spectrum actually softens roughly as much of the continuum as it hardens, and as a result, the net change to the shape of the continuum is very small.

A larger uncertainty is associated with the Lyman valley correction. Many parameters go into the correction, including those describing the shape of the H I column density distribution function ($\beta(N)$ in Equation 1), the minimum and maximum

TABLE 1
FITTED POWER-LAW INDICES

Radio	Redshift Range	Number spectra	Number objects	$\langle z \rangle$	$\langle L \rangle$	α_{NUV}	α_{EUV}	α_{EUV}
All	All	332	184	1.17	46.16	-0.69 ± 0.06	-1.71 ± 0.13	-1.76 ± 0.12
RL	All	205	107	1.00	46.01	-0.67 ± 0.08	-1.89 ± 0.15	-1.96 ± 0.12
RQ	All	127	77	1.42	46.38	-0.72 ± 0.09	-1.53 ± 0.16	-1.57 ± 0.17
RL	$z < 1.5$	190	94	0.84	45.91	-0.67 ± 0.08	...	-2.00 ± 0.09
RQ	$z < 1.5$	79	45	0.84	46.03	-0.72 ± 0.08	...	-1.70 ± 0.12
<hr/>								
Z97								
All	All	184	101	0.93	...	-0.99	-1.96	-2.02*
RL	All	110	60	0.87	...	-1.02	-2.16	-2.45*
RQ	All	74	41	0.95	...	-0.86	-1.77	-1.83*

*Z97 obtained these indices by fitting above 600 Å.

column densities, the redshift evolution parameter (γ in Equation 1), the proportionality constant in Equation 1, and the mean b parameter of the Lyman forest absorbers. Of these parameters, those with uncertainties that could most affect our results are the high-end cutoff column density and the redshift evolution parameterization.

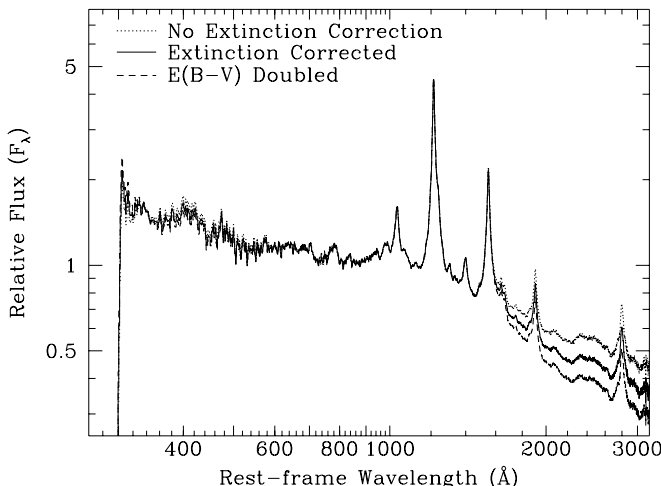


FIG. 5.— Overall composite (solid line), plotted along with the composite resulting from applying no extinction correction (dotted line) and that resulting from doubling all values of $E(B-V)$ (dashed line). The composites are virtually indistinguishable in the EUV.

As we discussed in §2.2, we correct statistically for all Lyman forest absorbers with $N(HI) < 10^{16.7} \text{ cm}^{-2}$, since we have corrected for larger column density absorbers individually. However, we are not certain of being complete down to $10^{16.7} \text{ cm}^{-2}$, and it could be that in fact a different limit is appropriate. We tried increasing and decreasing the limit by 50%, thus encompassing the range $10^{16.5} - 10^{16.9} \text{ cm}^{-2}$, and found that α_{EUV} in the total composite measured above 500 Å varied from -1.79 to -1.72 . The error associated with the maximum column density is therefore at most of the order ± 0.04 , so we take this as a liberal estimate of this error.

More poorly determined than the shape of the column density distribution function is its evolution with redshift, usually parameterized by a power-law index γ as in Equation 1, or more generally $\gamma(z)$. Low redshift studies with HST have shown that γ is small for $z < 1.5$, indicating very little evolution (Bahcall

et al. 1996; Impey et al. 1996). However, since the number of systems at low redshift is so much smaller than for $z \gtrsim 2$, we concern ourselves only with the evolution at higher redshift. For $z > 2$, accessible with ground-based spectroscopy, a large range in γ has been found, generally falling in the range 1.8–3.0, depending on the data and the details of the analysis (Zuo & Lu 1993; Bechtold 1994; Cooke, Espey, & Carswell 1997; Kim et al. 1997). We chose $\gamma = 2.46$ from Press et al. (1993) because it comfortably falls within the range of measured values. To determine the effect of γ on the result, we also tried $\gamma = 2.1$ and $\gamma = 2.8$, which resulted in α_{EUV} above 500 Å in the total composite of -1.73 and -1.78 , respectively. We therefore estimate the error at around ± 0.03 .

The errors in α_{EUV} listed in Table 1 include the bootstrap errors and the errors associated with the Lyman valley correction as discussed above. The errors in α_{NUV} reflect only the bootstrap uncertainty, as this portion of the continuum is unaffected by the Lyman valley.

One may also wonder whether any individual objects could have a significant influence on the composite. In fact, the well-studied QSO HE 2347-4342 has such an extremely hard EUV continuum that it does have a pronounced effect on the composite. Removing it from the overall sample softens the EUV power-law index, as fit above 500 Å, from -1.75 to -1.82 . This effect is already accounted for in the errors in Table 1, since it is precisely this source of uncertainty that we are measuring with the bootstrap resampling technique. However, the effect of HE 2347-4342 on the composite raises the question of whether or not this sample is representative of the whole QSO population. We return to this point in §5.

4.3. Luminosities

We estimate luminosities for the objects for the purpose of characterizing the sample. Since the continuum turns over in the region $\sim 1250 \text{ \AA}$, from $\alpha > -1$ above the break to $\alpha < -1$ below, the energy distribution peaks near the break. We therefore use λL_λ at 1100 \AA as our estimator of the luminosity. Since not all spectra include 1100 \AA , we use the composite as a template for estimating the flux at this wavelength. We calculate the ratio of each spectrum to the composite over the same wavelength range, then assume that this ratio also indicates the ratio

of the fluxes at 1100 Å. Thus, we use the following:

$$L_\lambda(1100\text{Å}) = F_c(1100\text{Å}) \frac{\sum_i F_{s,i}}{\sum_i F_{c,i}} 4\pi D_L^2, \quad (5)$$

where F_c is the flux in the composite, F_s is the flux in the individual spectrum, and the summation is over the wavelength coverage of the spectrum, excluding the emission line windows defined previously. For an $\Omega_\Lambda = 0$ universe, the luminosity distance D_L is given by the following formula first derived by Mattig (1958):

$$D_L(z) = \frac{2c}{H_0 \Omega_0^2} \{ \Omega_0 z + (\Omega_0 - 2)[(\Omega_0 z + 1)^{1/2} - 1] \}, \quad (6)$$

where we adopt $\Omega_0 = 1$ and $H_0 = 60 \text{ km s}^{-1} \text{ Mpc}^{-1}$. This yields a luminosity for each spectrum. For objects for which there is just one spectrum, that luminosity is assigned to the object. For those with more than one spectrum, if one of the spectra contains 1100 Å, the luminosity obtained from that spectrum is assigned to the object, otherwise the luminosity from the spectrum with wavelength coverage closest to 1100 Å is used. In Figure 6 we plot the luminosities of all the objects in our sample as a function of redshift. The strong correlation of luminosity with redshift characteristic of flux-limited samples is apparent here. It is interesting to note the distribution of radio-loud and radio-quiet objects with redshift. At intermediate redshifts, $0.6 < z < 1$, the sample is dominated by radio-loud QSOs, whereas for $z \gtrsim 1.5$, the sample is mostly radio-quiet. As a result, at longer wavelengths, the overall composite is dominated by radio-loud data, while at shorter wavelengths (specifically, $\lambda \lesssim 900 \text{ Å}$) the composite contains more radio-quiet data than radio-loud.

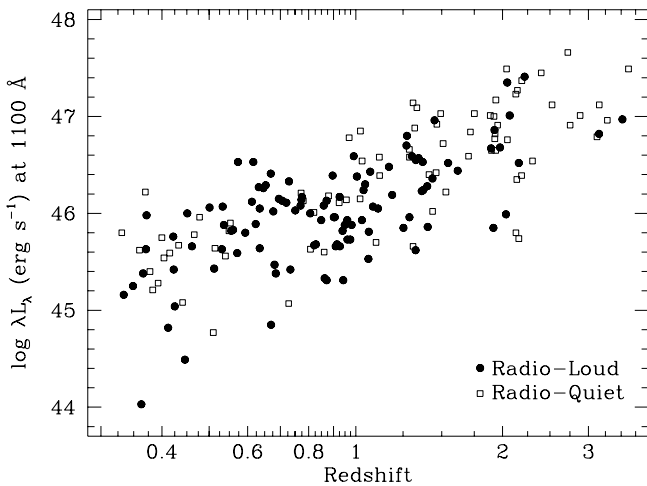


FIG. 6.— Distribution of QSOs in redshift and monochromatic luminosity at 1100 Å. Filled circles are radio-loud objects, open squares are radio-quiet.

4.4. Radio properties

Given the large numbers of each at our disposal, we separate the sample into radio-loud and radio-quiet subsamples to investigate the radio dependence. The analysis of each subset is done as it was for the full composite, creating the composites with a bootstrap and fitting with a broken power law. The bootstrap errors were also computed independently for each sample as for the full composite. The full radio-loud and radio-quiet composites are plotted in Figures 7 and 8, and the power-law indices

are listed in Table 1. The radio-loud composite has a significantly softer EUV continuum than the radio-quiet composite, although the NUV continua are virtually identical. However, as is evident in Figure 6, the distribution of objects with redshift is quite different for the two groups above $z \gtrsim 1.5$. We therefore repeated the analysis using only objects for which $z < 1.5$, for which the distributions in redshift and luminosity are quite similar. The results are also listed in Table 1. The difference between the two is still substantial although somewhat smaller for $z < 1.5$ than for the full composites, primarily due to the exclusion of HE 2347-4342 from the radio-quiet sample. Using the bootstrap resampling distributions used to compute the errors on α_{EUV} , we estimate that the radio-loud composite is softer than the radio-quiet composite with 98.6% confidence.

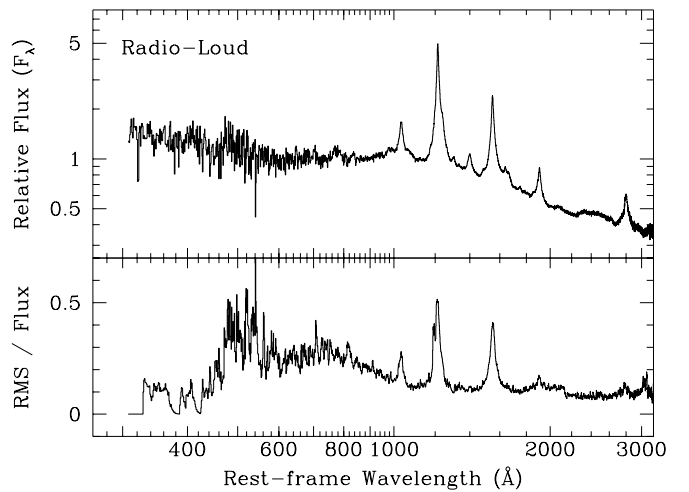


FIG. 7.— Radio-loud composite spectrum (above) and corresponding relative RMS deviation from the mean for each 1 Å pixel (below). The RMS deviation has been smoothed by five pixels.

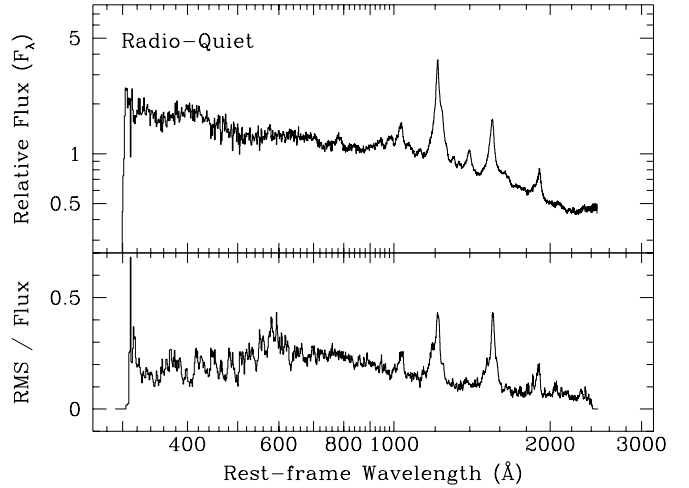


FIG. 8.— Same as Figure 7 for the radio-quiet composite.

4.5. Spectral Variations

In addition to the mean composites, we also plot in Figures 7 and 8 the RMS deviation of the individual spectra about the mean in 1 Å bins for the radio-loud and radio-quiet subsamples, respectively, smoothed by five pixels and normalized to the composite flux. The RMS deviations in the two groups are very similar, differing significantly only where the number of

contributing objects is small. The RMS spectra consist mostly of an RMS “continuum” caused by a combination of differences in continuum shapes and noise, both Poisson noise and that resulting from intervening absorption. The RMS continuum increases towards shorter wavelengths down to ~ 700 Å, where the Lyman valley correction peaks. Shortward of this, there are large fluctuations in the RMS deviation as the number of contributing objects becomes small. Above the continuum, one can see the effects of the variation in the strong emission lines, particularly O VI, Ly α , and C IV. By subtracting in quadrature the RMS continuum from the emission line RMS values, we can estimate the RMS deviation in the strength of the emission lines. The features in Figures 7 and 8 correspond to RMS fluctuations in the peak emission-line flux in O VI, Ly α , and C IV of ~ 50 –70%.

4.6. Emission Lines

To aid in making likely identifications of the emission lines in our composites, we generate a few simple broad-line region models using typical parameters with the photoionization code CLOUDY (version 94.00; Ferland 1996). We use single-slab models of a broad-line region with solar abundances, densities of 10^8 to 10^{10} cm $^{-3}$, and total column densities from 10^{23} to $10^{25.5}$ cm $^{-2}$. We assume the broad-line region is illuminated by a power-law continuum with index α_ν , from -1.5 to -1.8 and an ionization parameter ranging from $\log U = -2.0$ to 0.0 . We look for the strongest lines in the models, those with fluxes greater than ~ 0.001 times H β , and consider these to be the most plausible identifications. For the plentiful transitions of Fe II, Fe III, Si II, and Si III, we use as a guide the identifications made in the SDSS composite (Vanden Berk et al. 2001) and in the narrow-line quasar 1 ZW 1 (Laor et al. 1997b).

The composite is shown in Figures 9 and 10 with all of the identified emission lines between 600 and 2000 Å labeled. We now make some brief comments on a few features:

1. There is an odd feature at ~ 700 Å, a slight change in flux that looks like it could be partly due to an emission line, which we tentatively identify as O III $\lambda 703$. We have tried changing the details of the composite construction process, including the direction of the bootstrapping, the weighting of the individual spectra, and the emission line masking windows, but the feature always appears. It therefore seems unlikely that this is due to a problem with our procedure, such as improper normalization of the spectra. Also, there are more than 40 spectra contributing at this wavelength, so the feature should not be due to any single object, and we have explicitly checked that this is the case. Thus, it seems that this feature is representative of the sample spectra.
2. We identify the feature at ~ 774 Å as primarily Ne VIII as has been previously reported (Hamann, Zuo, & Tytler 1995; Hamann et al. 1998). However, the models predict some O IV $\lambda 789$ to be present, and the appearance of the Ne VIII feature as being skewed and shifted to the red suggests that O IV may contribute.
3. A broad feature from ~ 900 to ~ 950 Å appears in the composite that we identify as collected emission of many H I Lyman lines of order Ly δ and higher, possibly blended with S VI $\lambda\lambda 933, 945$. The He II Balmer series

could contribute, but due to the lack of evidence for emission from He II Ba7 at 959 Å, we conclude that it is unimportant.

4. Redward of O VI at around 1065 Å appears a broad feature that can only partially be explained by N II and He II at 1085 Å. Z97 tentatively identified this feature as Ar I $\lambda 1067$. We find no definitive identification, though it could be due to an Fe II blend visible in the theoretical Fe II simulations of Verner et al. (1999). Another possible identification is S IV $\lambda\lambda 1063, 1073$ (Zheng et al. 2001).
5. There is a weak emission feature at ~ 1347 Å that we cannot identify. A similar feature was observed by Laor et al. (1997b).

To measure the strength of the emission features we fit them with Gaussian components using *specfit*. The resulting emission-line fluxes and equivalent widths are listed in Table 2, as well as the results for the radio-loud and radio-quiet composites. We do not quote the errors in equivalent width because the relative errors are the same as for the fluxes. The fluxes are normalized to a flux of 100 for Ly α . In producing the fits, we use the simplest model possible while still providing a good fit to the data.

The spectrum is fit in five pieces: 730–1150 Å, 1140–1323 Å, 1318–1705 Å, 1700–2215 Å, and 2100–3020 Å. Each section is fit with a power-law continuum plus Gaussian components. Mg II, C III], Si IV + O IV], C IV, N V, and O VI are all fit with two Gaussian components, a broad one and a narrower one, with the peak wavelengths of the two components fixed to each other. Ly α requires an additional narrow component for a good fit. In fitting the Ly α / N V feature, the wavelength ratio of the Ly α to the N V components is fixed at its laboratory value, and the widths of the N V components are bound to the widths of the broader two Ly α components. The wavelength ratios of Ly β to O VI and Si III] to C III are fixed in the same way. Because the C IV profile is so skewed, especially in the radio-quiet composite, it is necessary to fit C IV with a skewed Gaussian where the skew parameters of each of the components are bound together. All of the remaining features are fit with a single Gaussian component, including Ne VIII + O IV, the broad feature at ~ 930 Å, C III + N III, Si IV + O IV], and the broad feature longward of O VI including N II and He II. Ne VIII + O IV and the H I Lyman feature were also skewed to provide a good fit. The addition of a very broad feature (FWHM ~ 25000 km s $^{-1}$) at ~ 1600 Å, perhaps due to Fe II emission or a very broad component (VBC) of C IV, is necessary to provide a good fit to the C IV blend. This component comprises a rather large amount of flux, more than half that of C IV. The resulting decomposition of the C IV blend is quite similar to that performed by Laor et al. (1994) on similar data. We quote summed values for some blends where the deblending is highly uncertain. For some of the weaker lines, the values for the overall composite do not fall in between those for the radio-loud and radio-quiet composites, a result of some uncertainty in the modeling not reflected in the quoted errors.

In addition to comparing line strengths of the radio-loud and radio-quiet composites, it is instructive to compare the spectra directly. We have plotted the radio-loud and radio-quiet composites together in Figures 9 and 10. The ratios of the two are shown in the bottom panels of the figures.

TABLE 2
EMISSION LINES

Line	λ_0 (Å)	Whole Sample		Radio Quiet		Radio Loud	
		Flux	EW (Å)	Flux	EW (Å)	Flux	EW (Å)
Ne VIII + O IV	~ 780	5.2 ± 0.2	4.4	5.7 ± 0.2	4.3	4.7 ± 0.3	4.1
O III	835	1.1 ± 0.1	1.0	1.5 ± 0.2	1.2	1.2 ± 0.1	1.0
H I Ly series + S VI	~ 930	5.1 ± 0.2	4.3	8.4 ± 0.3	6.6	3.1 ± 0.3	2.7
C III + N III	~ 980	11.3 ± 0.2	9.7	11.7 ± 0.2	9.4	8.1 ± 0.6	7.1
O VI + Ly β	~ 1030	18.0 ± 0.3	15.6	18.1 ± 0.9	14.6	19.1 ± 2.6	16.9
N II + He II + ?	~ 1065	5.2 ± 0.2	4.6	5.5 ± 0.2	4.5	5.6 ± 1.1	5.0
Fe III	1123	0.65 ± 0.06	0.57	2.2 ± 0.2	1.8	0.28 ± 0.04	0.25
C III*	1176	0.40 ± 0.05	0.36	0.43 ± 0.05	0.36	0.44 ± 0.03	0.39
Si II	~ 1195	1.02 ± 0.08	0.93	0.47 ± 0.09	0.40	1.5 ± 0.1	1.4
Ly α	1216	100.0 ± 0.8	91.8	100.0 ± 0.8	86.3	100.0 ± 0.7	91.2
N V	1240	20.0 ± 0.5	18.5	17.5 ± 0.6	15.4	22.0 ± 0.4	20.2
Si II	1263	0.32 ± 0.02	0.30	0.41 ± 0.03	0.37	0.27 ± 0.02	0.25
O I + Si II	~ 1305	2.03 ± 0.07	1.94	2.5 ± 0.1	2.3	1.9 ± 0.1	1.7
C II	1335	0.61 ± 0.05	0.60	1.0 ± 0.4	0.9	0.35 ± 0.03	0.34
?	1347	0.15 ± 0.02	0.15	0.3 ± 0.1	0.3	0.07 ± 0.02	0.07
Si IV + O IV]	~ 1400	9.4 ± 0.2	9.9	11.9 ± 1.3	12.2	8.6 ± 0.3	9.0
N IV]	1486	2.4 ± 0.1	2.7	0.6 ± 0.1	0.6	2.8 ± 0.1	3.2
C IV	1549	48.0 ± 0.4	58.0	38.0 ± 4.4	44.7	52.0 ± 0.2	62.9
broad feature	~ 1600	26.7 ± 0.5	34.6	25.9 ± 0.9	31.9	30.2 ± 0.4	38.5
He II	1640	1.11 ± 0.05	1.45	1.0 ± 0.5	1.3	1.19 ± 0.05	1.57
O III]	1664	1.79 ± 0.03	2.39	0.7 ± 0.6	1.0	2.25 ± 0.03	3.01
N III]	1750	0.44 ± 0.02	0.58	0.21 ± 0.02	0.26	0.50 ± 0.02	0.67
Al III	1857	1.49 ± 0.05	2.19	2.4 ± 0.1	3.3	1.20 ± 0.05	1.77
C III] + Si III]	~ 1900	12.9 ± 0.2	19.7	12.8 ± 0.4	18.5	13.2 ± 0.2	20.3
Fe II	~ 2185	1.7 ± 0.1	3.2	0.60 ± 0.04	1.1	1.8 ± 0.1	3.4
Mg II	2799	22.6 ± 0.2	51.7	22.3 ± 0.3	51.7

There are some noteworthy differences between the different radio composites. Francis et al. (1993) found that Ly α and C IV have both larger equivalent widths and stronger narrower peaks in radio-loud objects. We verify these results, except that the difference in Ly α equivalent width is quite moderate, only 6%. However, we note that the sample of radio-loud QSOs for which Francis et al. (1993) measured Ly α is quite small (only seven objects). The enhancement of the equivalent width of C IV, 41% larger in radio-loud QSOs than radio-quiet QSOs, agrees well with their results. Equivalent width enhancements for N V (31%) and O VI (16%) are also seen in our data. As can be seen in Figure 9, the tendency for a stronger narrow component in radio-loud objects may also apply to O VI, although much less than for C IV and Ly α .

Also notable is the difference in the distribution of the emission in velocity space. The profiles of O VI, Ly α , Si IV + O IV], C IV, and C III] all show a tendency for more emission to the red and less to the blue in radio-loud QSOs as opposed to radio-quiet. For C III], this could be due to a difference in the neighboring Si III] and Al III emission. Also, there are only twelve spectra contributing to the C III] profile in the radio-quiet sample, so this may not be a general property. For O VI, Ly α , and Si IV + O IV], this can be mostly explained by a systematic blueshift of the entire line emission in radio-quiet objects, an effect commonly observed in C IV (e.g., Marziani et al. 1996; Sulentic et al. 2000). However, in our data, the difference in C IV emission between radio-loud and radio-quiet objects appears to be due largely to a blue asymmetry in the radio-quiet profile shape, an effect which has also been reported (Wills et al. 1993).

There are other minor differences as well. The broad feature at ~ 930 Å is quite strong in the radio-quiet composite, but more than a factor of two weaker in the radio-loud composite. The Fe III $\lambda 1123$ feature is also much stronger in the radio-quiet composite, by roughly a factor of seven.

5. INDIVIDUAL OBJECTS

To explore in another way the difference in α_{EUV} between radio-loud and radio-quiet, as well as to search for correlations of α_{EUV} with redshift and luminosity, we fit α_{EUV} for all individual objects for which it is possible to do so using the same continuum windows as for the composite. In order to have a sufficient baseline for measuring α_{EUV} , we demand that to fit an object it must either have either (1) data above 1100 Å and data below 900 Å, or (2) continuous data from 700 Å to 900 Å. For a few objects, it was necessary to alter slightly the continuum windows, so as to avoid absorption features, in order to obtain a good fit. A few others had to be thrown out because absorption was too prevalent or the S/N was too low to obtain a good fit. For performing these fits for objects for which there are multiple spectra with continuous wavelength coverage, the individual spectra are combined into a single spectrum.

The histograms of α_{EUV} for the 40 radio-loud and 39 radio-quiet objects that could be fit are shown in Figure 11. The mean, median, and standard deviation of these distributions are listed in Table 3. We estimate the errors on the mean and median for each distribution by again using the bootstrap resampling method, except that for the median we use the half-sample method, which is a better estimator for the error on the median (Babu 1992). The means and medians of the distributions agree

TABLE 3
INDIVIDUAL OBJECT FITS

Group	N	Mean		Median	RMS	α_{EUV} vs. $\log z$			α_{EUV} vs. $\log L$		
		α_{EUV}	α_{EUV}			r	Signif.	Slope	r	Signif.	Slope
RQ	39	-1.61 ± 0.14	-1.59 ± 0.06	0.86	0.118	0.527	0.09 ± 0.56	-0.004	0.017	-0.03 ± 0.27	
RL	40	-1.95 ± 0.11	-1.95 ± 0.12	0.66	-0.119	0.534	-0.33 ± 0.66	0.271	0.909	0.63 ± 0.27	

well with the indices fit to the composites, which argues that the composites are indeed representative of their constituent spectra. A two-population Kolmogorov-Smirnov test shows that the distribution of α_{EUV} for the radio-loud and radio-quiet objects are different with 98.6% confidence.

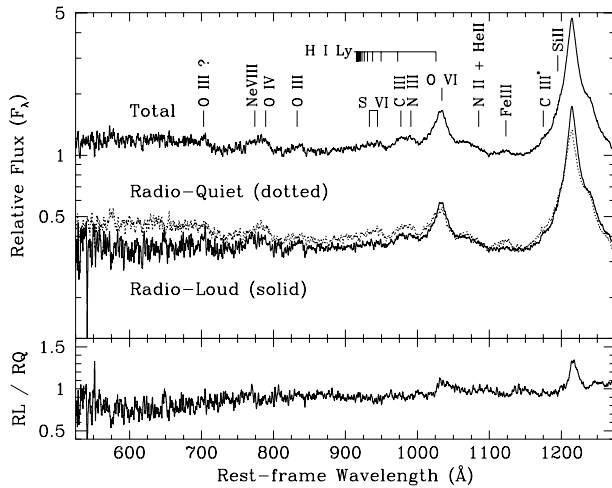


FIG. 9.— The top panel shows the overall composite below Ly α with identified emission lines marked. Below the overall composite are the radio-loud composite (solid line) and the radio-quiet composite (dotted line), normalized to have the same flux at ~ 1100 \AA . The bottom panel shows the ratio of the radio-loud composite to the radio-quiet composite.

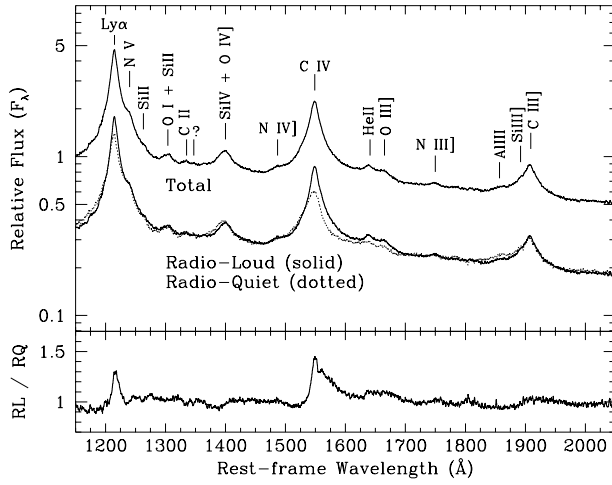


FIG. 10.— Same as Figure 9 for the spectral region from Ly α to 2050 \AA . The radio-loud and radio-quiet composites are normalized to have the same flux at 1450 \AA . Differences in the profiles of the strong broad lines are evident, particularly for C IV.

The objects are plotted in the redshift- α_{EUV} parameter space in Figure 12, and likewise they are plotted in the luminosity-

α_{EUV} parameter space in Figure 13. To test if there is any correlation between α_{EUV} and either redshift or luminosity, we calculate the Spearman rank-order correlation coefficient r and its significance for each relation, listed in Table 3. Only one relation, α_{EUV} vs. luminosity for radio-loud objects, shows any evidence for a correlation, and only marginally so, at the $\sim 90\%$ confidence level. To place limits on the possible range of any variation of α_{EUV} with redshift or luminosity for comparison with the literature, we fit α_{EUV} vs. $\log z$ and α_{EUV} vs. $\log L$ using a standard least-squares linear regression. The best fit slopes and errors are also shown in Table 3. Consistent with the rank-order correlation test, all of the slopes are consistent with zero with the exception of α_{EUV} vs. $\log L$ for the radio-loud objects.

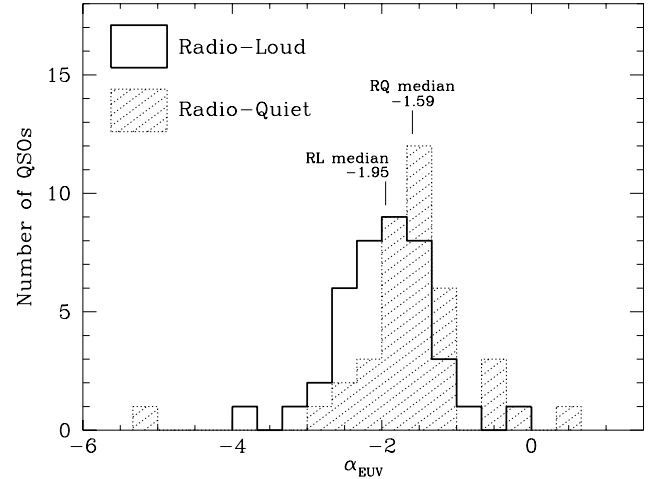


FIG. 11.— Histogram of EUV power-law indices in bins of 0.33 for 40 radio-loud and 39 radio-quiet QSOs. The means, medians, and RMS deviations of the distributions are listed in Table 3.

In Figures 12 and 13 we have labeled three objects that are noteworthy for their extreme values of α_{EUV} . The hardest EUV spectrum is that of HE 2347-4342 with an α_{EUV} of +0.56. The conspicuously hard UV spectrum, which results in HE 2347-4342 being quite bright far into the EUV, has made this object a favorite for studying He II Ly α absorption in the IGM (Reimers et al. 1997; Kriss et al. 2001). Two other objects have quite soft EUV spectra, the radio-loud QSO MC 1146+111 and the radio-quiet QSO TON 34. As can be seen in Figure 13, MC 1146+111 is by far the least luminous QSO for which we measure α_{EUV} , so it is perhaps not surprising that it is an outlier, particularly given the suggestion of a luminosity dependence for radio-loud objects. TON 34 is quite extreme, with a measured α_{EUV} of -5.29. The object appears quite normal in the optical (Sargent, Steidel, & Boksenberg 1988). Data from the International Ultraviolet Explorer seem to confirm this continuum shape down to 2200 \AA , where the HST data end, although it appears that the

spectrum may flatten at shorter wavelengths (Tripp, Bechtold, & Green 1994). We note that the QSO UM 675 has a very similar continuum shape to TON 34, although it did not quite meet our stipulated requirements to measure α_{EUV} . These objects may be affected by intrinsic reddening by dust in the vicinity of the QSO.

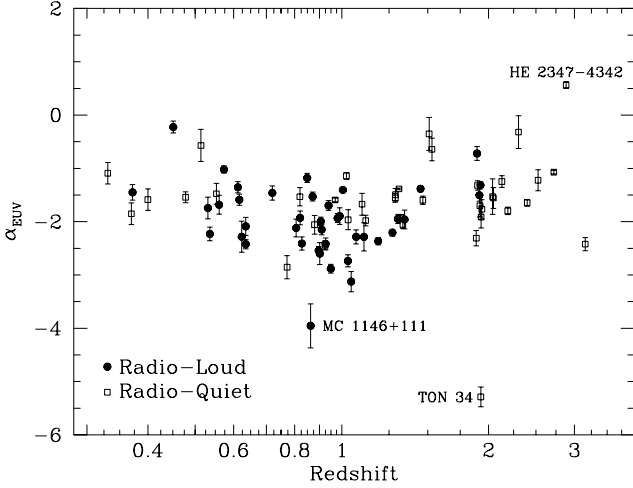


FIG. 12.— Individual EUV power-law indices for all objects for which it could be measured, plotted against redshift.

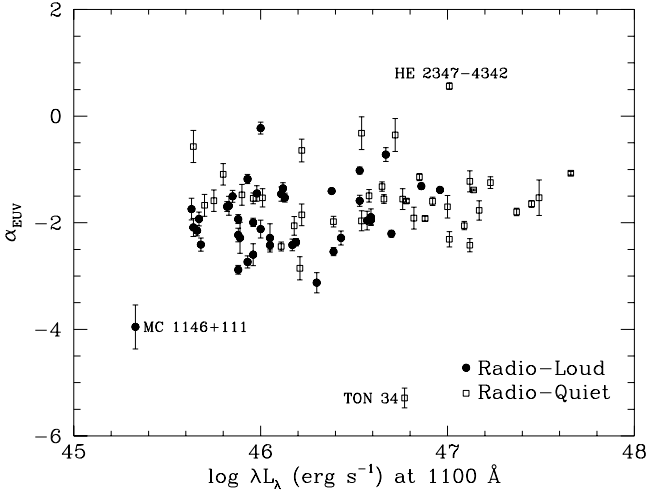


FIG. 13.— Individual EUV power-law indices for all objects for which it could be measured, plotted against monochromatic luminosity at 1100 Å.

For the objects for which we measured α_{EUV} , we have also measured α_{NUV} when possible. Because very few objects have HST data both below 900 Å and above 2000 Å, we cannot fit α_{NUV} in exactly the same way as the composite. To define the fit better, we add additional fit windows: 1315–1325, 1350–1365, 1450–1470, 1760–1840. We obtain fits of α_{NUV} for 11 radio-quiet and 19 radio-loud objects, plotted against α_{EUV} in Figure 14. Clearly, there is no correlation between α_{NUV} and α_{EUV} ; the significance of any correlation from the Spearman rank-order test is 0.055.

In light of a lack of correlation of α_{NUV} with α_{EUV} , we return to the subject of bias in our sample; specifically, whether our sample is a representative one in the EUV. The objects for which we measure α_{EUV} , by definition, are at redshifts that place the EUV continuum in the observed-frame UV. These ob-

jects are generally selected for UV spectroscopy by their brightness in the optical, or the rest-frame NUV region. Thus, if there is a bias, one would expect it to be primarily towards harder α_{NUV} , as these objects will be brighter in the observed UV. However, since Figure 14 suggests no correlation, we conclude that any bias in α_{NUV} should not translate into a bias in α_{EUV} , and thus our sample is likely to be representative of the overall population, except at the shortest wavelengths (see §4.1).

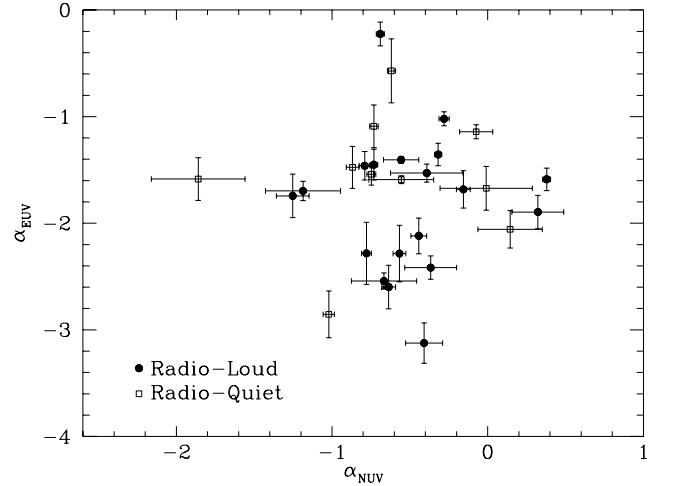


FIG. 14.— Individual EUV power-law indices vs. NUV power-law indices, for all objects for which both could be measured.

6. DISCUSSION

6.1. Optical Composites

As a basis for comparison of our work to optical composites, we compare our radio-quiet composite to the SDSS composite (Vanden Berk et al. 2001). For our purposes, differences among the comprehensive optical composites are small and have been studied by other authors (Brotherton et al. 2001; Vanden Berk et al. 2001). Vanden Berk et al. (2001) quote a power-law index in their median composite between Ly α and 4000 Å, equivalent to what we call α_{NUV} , of -0.46 , significantly harder than our value of -0.71 . This can be partially explained by the way in which this value is measured. Because we do not have data to such long wavelengths as the SDSS composite, the longest wavelength windows we use to estimate the continuum are at 1975–2000 and 2150–2200 Å, much shorter than the wavelengths spanned by the SDSS composite. In our composite these appear to be free of emission lines. However, a longer continuum baseline as is available for the SDSS composite suggests that even these windows are contaminated by Fe II emission, which would cause us to infer a softer continuum. If we measure the spectral index of the SDSS composite in the same way as we have done, we get $\alpha_{NUV} = -0.53$, partially explaining the discrepancy.

The remainder of the difference must come from a genuine difference between the spectra. In Figure 15, we plot our radio-quiet composite along with the SDSS composite, with the two normalized to the same flux at 1450 Å. The bottom panel shows the ratio. Clearly, there is a slight slope to the ratio of the spectra, confirming that a genuine difference exists. This difference is likely due to the fact that at any given wavelength, the mean redshift of objects contributing to our composite is significantly less than for the SDSS composite. The difference in

α_{NUV} can thus be attributed to both a true evolution of QSOs to softer spectra at lower redshift as well as an observational bias towards detecting QSOs with harder spectra at high redshift (Francis 1993).

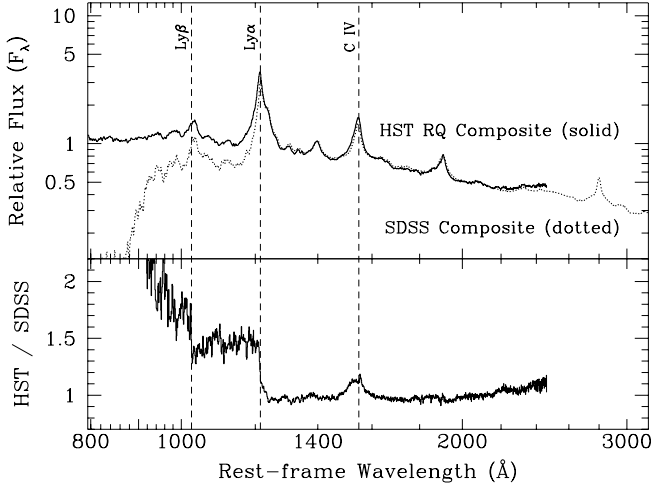


FIG. 15.— Above, our HST RQ composite compared to the SDSS composite, where the two have been normalized to have the same flux at ~ 1450 Å. Below, the ratio of the HST composite to the SDSS composite. The sharp features at Ly α and Ly β are due to intervening Lyman-line absorption. Excess C IV emission is evident.

Only two other major differences are evident in Figure 15. The first is the discontinuities at the positions of Ly α and Ly β due to intervening Lyman line opacity. Our composite does not show these features because we have corrected for line opacity, but even if we had not the discontinuities would be much weaker, owing to the much lower density of intervening absorbers at lower redshift. The other obvious feature is an excess of C IV emission in our composite relative to the SDSS. This is likely due to the known tendency of high-ionization emission lines to have lower equivalent widths at higher luminosity, the so-called Baldwin effect (Baldwin 1977).

6.2. The EUV / X-Ray Continuum

For radio-quiet QSOs, our results are in excellent agreement with the existence of a common power-law continuum describing the entire EUV / soft X-ray spectral energy distribution from ~ 10 eV to 2 keV. The ratio of optical to X-ray flux is conventionally represented by the effective power-law index α_{ox} , defined as $\alpha_{ox} = (l_o - l_x)/2.605$, where l_o and l_x are the common logarithms of the monochromatic fluxes in units of $\text{erg cm}^{-2} \text{s}^{-1} \text{Hz}^{-1}$ at 2500 Å and 2 keV, respectively. Assuming the continuum shape of our composite to convert from λL_λ at 1100 Å to l_o , the QSOs in our sample fall in the range $30 \lesssim l_o \lesssim 32.5$. Typical mean values of α_{ox} from samples of QSOs at these luminosities tend to fall in the range 1.5–1.6 (Anderson & Margon 1987; Avni, Worrall, & Morgan 1995; Green et al. 1995; Yuan et al. 1998). Assuming the NUV spectral shape of our composite and extrapolating the composite EUV continuum with α_{EUV} of -1.57 ± 0.17 to 2 keV, we would expect an α_{ox} of 1.50 ± 0.15 , consistent with the measurements of α_{ox} . Although we find no correlation of α_{EUV} with luminosity for radio-quiet objects (§5), our limits on the slope are consistent with the slight dependence of α_{ox} on luminosity ($d\alpha_{ox}/dl \approx 0.1$) found in X-ray studies of optically-selected AGN (Kriss & Canizares 1985; Avni et al. 1995). Our finding

of no evolution with redshift is also consistent with these studies. In addition, our EUV continuum shape matches well with the typical soft X-ray continuum slope of low-redshift QSOs. Laor et al. (1997a) find a mean α_x of 1.72 ± 0.09 for a sample of $19 z < 0.4$ radio-quiet QSOs, while Yuan et al. (1998) find a mean α_x of 1.58 ± 0.05 for a much larger sample of $146 z < 0.5$ radio-quiet QSOs. Thus both the typical continuum shape and luminosity of radio-quiet QSOs in the soft X-ray region are in good agreement with an extrapolation of our results to higher energies.

The situation is more complicated for radio-loud QSOs. While an extrapolation of our EUV continuum with $\alpha_{EUV} = -1.96 \pm 0.12$ yields $\alpha_{ox} = 1.84 \pm 0.10$, data show that radio-loud QSOs are much more luminous in the soft X-ray band than this extrapolation. Brinkmann, Yuan, & Siebert (1997) find a mean value of α_{ox} of 1.24 for flat spectrum sources and 1.33 for steep spectrum sources. They also find typical power-law indices in the soft X-ray ~ -1.0 , although this is found to depend on the properties of the radio emission. Thus radio-loud QSOs are both much too luminous and too flat in the soft X-ray to be explained as an extrapolation of the EUV emission, and there must be some significant change in spectral shape somewhere between ~ 50 eV and a few tenths of a keV, corresponding to the limits of the studied portions of the rest-frame EUV and soft X-ray bands.

The apparent existence of a common EUV / X-ray continuum in radio-quiet QSOs results in a return of the problem for which the EUV bump of Mathews & Ferland (1987) was hypothesized; specifically, the observed strength of He II $\lambda 1640$ emission. Assuming $\alpha_{EUV} = -2$, Korista, Ferland, & Baldwin (1997) pointed out that it is difficult to generate the observed amount of He II $\lambda 1640$ emission with such a soft ionizing spectrum. In terms of an ensemble property of radio-quiet QSOs, our currently favored value of $\alpha_{EUV} = -1.57$ lessens this problem somewhat by providing nearly twice as many photons at 4 Ryd. Scaling the calculations of Korista et al. (1997), assuming as they did a covering fraction of 10%, we would expect a He II $\lambda 1640$ EW of $\sim 1\text{--}2$ Å, where this range takes into account some uncertainty in the modeling and our error on α_{EUV} . This estimate in fact agrees well with our measured value of 1.3 Å. However, in our decomposition of the C IV blend we have made a conservative measurement of the He II $\lambda 1640$ emission, fitting only the well-defined core of the line above the broad ~ 1600 Å feature, and our value is low in comparison to typical values measured for individual objects using more detailed methods, even those obtained from many of the same spectra that comprise our sample (Laor et al. 1995; Marziani et al. 1996). If any significant amount of flux from the ~ 1600 Å feature belongs to a broader component of He II $\lambda 1640$, we may be underestimating the flux by up to a factor of several, which cannot be easily explained with our proposed ionizing continuum.

6.3. Ionization of the Intergalactic Medium

The observation of strong absorption by He II Ly α $\lambda 304$ Å in high-redshift QSO spectra (Jakobsen et al. 1994; Davidsen, Kriss, & Zheng 1996; Reimers et al. 1997) have shown that the bulk of the IGM is in a highly-ionized state. This is generally believed to be due to photoionization by integrated EUV radiation from QSOs and/or hot, massive stars. Because radio-quiet QSOs are much more common than their radio-loud counterparts (e.g., Sramek & Weedman 1980; Condon et al. 1981), the radio-quiet QSO spectral energy distribution is generally taken

as representative of the QSO population, so we use our radio-quiet value of $\alpha_{EUV} = -1.57 \pm 0.17$ to compare to the literature. Many models of the ionization of the IGM (Haardt & Madau 1996; Fardal, Giroux, & Shull 1998, Madau, Haardt, & Rees 1999) assume the dominant source of the metagalactic ionizing is QSOs, although the latter two articles discuss the contribution of stars (see also Madau & Shull 1996; Haehnelt et al. 2001). These models assume that the QSO ionizing radiation is emitted as a pure power law but is subsequently reprocessed through absorption and reemission by the intergalactic gas.

Kriss et al. (2001) have recently completed a detailed analysis of a Far Ultraviolet Spectroscopic Explorer (FUSE) spectrum of HE 2347-4342 that provides data on the He II Ly α forest for $2.3 < z < 2.7$. They attribute the He II absorption entirely to discrete absorbers and find a large range in the ratio of He II to H I column densities (η) of these absorbers, from $\eta = 1$ to $\eta > 1000$, with a mean value of $\langle \eta \rangle = 78 \pm 7$. Comparing to the models of Fardal et al. (1998), $\alpha_{EUV} = 1.57 \pm 0.17$ would lead to values of η in the range 25–60. This is consistent with the lower values in the observed range of η , but it cannot explain the highest values observed. However, as is evident in Figure 11, individual radio-quiet QSOs show a wide spread in α_{EUV} with an RMS deviation of 0.86. Deviations of this magnitude from the mean would correspond to a range of η from $\eta < 10$ to $\eta > 100$ according to the Fardal et al. (1998) models. Although there is considerable uncertainty in the modeling due to the many input parameters involved, and the uncertainty on our measurement of α_{EUV} is substantial, it is possible that the typical QSO spectrum is somewhat too hard to explain the highest values of η (> 1000) observed in the IGM, and an additional source of hydrogen ionizing photons, such as starburst galaxies, may be necessary to soften the metagalactic ionizing radiation.

7. SUMMARY

We have studied the UV spectral properties of QSOs using 332 HST spectra of 184 $z > 0.33$ QSOs. This sample is nearly a factor of two larger than that of Z97, with the largest improvement coming in the 600–800 Å range, where our composite is composed of up to five times as many spectra as that of Z97. We confirm the result of Z97 that the UV spectral continuum can be approximated by a broken power law with the break in the vicinity of Ly α . However, we find a somewhat harder continuum than Z97. For the overall composite, we find a continuum power-law index between 500 Å and the break of $\alpha_{EUV} = -1.76 \pm 0.12$. For the subset of exclusively radio-loud objects, we find $\alpha_{EUV} = -1.96 \pm 0.12$; for the radio-quiet sub-

set, $\alpha_{EUV} = -1.57 \pm 0.17$. Based on the bootstrap technique of resampling the spectra to generate the likely distributions of the measured values of α_{EUV} , we find that the radio-quiet QSOs have harder EUV spectra than radio-loud QSOs with 98.6% confidence.

To verify that the composite is representative of the sample spectra, we measure α_{EUV} for as many individual objects as possible in the same manner as for the composite. We find median values of α_{EUV} of -1.59 for the radio-quiet QSOs and -1.95 for the radio-loud QSOs, in excellent agreement with the composites. We apply a two-population Kolmogorov-Smirnov test to the two distributions of α_{EUV} , with the result that the radio-loud and radio-quiet values were not drawn from the same parent distribution with 98.6% confidence. Also, we use these data on individual objects to search for dependencies of α_{EUV} on luminosity or redshift. We find no evidence for evolution of α_{EUV} with redshift for either radio-loud or radio-quiet QSOs. We also find no evidence for a correlation between α_{EUV} and luminosity for radio-quiet QSOs, though the limits are consistent with the slight increase of α_{ox} with increasing luminosity found in some X-ray studies. The radio-loud QSOs indicate a possible correlation with luminosity, with the trend being towards harder spectra with increasing luminosity. A Spearman rank-order correlation test indicates that the correlation is real with 90.9% confidence.

An extrapolation of our radio-quiet composite to higher energies is in good agreement with X-ray data, indicating that it is plausible to represent the entire typical ionizing continuum from ~ 10 eV to ~ 2 keV by a single power law. However, radio-loud QSOs are in general both flatter and more luminous in soft X-ray regime than an extrapolation of our composite, suggesting that there should be a change in spectral shape between the EUV and soft X-ray regions. The fact that radio-quiet QSOs may be represented by a single power law with spectral index $\alpha_{EUV} = -1.57 \pm 0.17$ is roughly in agreement with models of the IGM being photoionized by integrated QSO radiation as filtered by intergalactic material, given the uncertainty of our result and those of the models. However, as recent results show that at least some regions of the IGM are photoionized by even softer spectra, it is possible that an additional source of soft ionizing radiation, such as hot, massive stars, may be necessary to fully explain the ionization state of the IGM.

This research has been supported by grant AR-07977.01-96A from the Space Telescope Science Institute, which is operated by the Association of Universities of Research in Astronomy, Inc., under NASA contract NAS5-26555.

REFERENCES

Anderson, S. F. & Margon, B. 1987, ApJ, 314, 111
 Avni, Y., Worrall, D. M., & Morgan, W. A. 1995, ApJ, 454, 673
 Babu, G. J. 1992, Ann. Inst. Statist. Math., 44, 703
 Bahcall, J. N. et al. 1996, ApJ, 457, 19
 Baker, J. C. & Hunstead, R. W. 1995, ApJ, 452, L95
 Baldwin, J. A. 1977, ApJ, 214, 679
 Bechtold, J. 1994, ApJS, 91, 1
 Brinkmann, W., Yuan, W., & Siebert, J. 1997, A&A, 319, 413
 Brotherton, M. S., Tran, H. D., Becker, R. H., Gregg, M. D., Laurent-Muehleisen, S. A., & White, R. L. 2001, ApJ, 546, 775
 Cardelli, J. A., Clayton, G. C., & Mathis, J. S. 1988, ApJ, 329, L33
 Condon, J. J., Odell, S. L., Puschell, J. J., & Stein, W. A. 1981, ApJ, 246, 624
 Cooke, A. J., Espey, B., & Carswell, R. F. 1997, MNRAS, 284, 552
 Davidsen, A. F., Kriss, G. A., & Zheng, W. 1996, Nature, 380, 47
 Dinshaw, N., Foltz, C. B., Impey, C. D., & Weymann, R. J. 1998, ApJ, 494, 567
 Fardal, M. A., Giroux, M. L., & Shull, J. M. 1998, AJ, 115, 2206
 Ferland, G. J. 1996, Hazy, a Brief Introduction to Cloudy, Univ. Kentucky, Dept. Physics & Astron. Internal Rep.
 Francis, P. J. 1993, ApJ, 407, 519
 Francis, P. J., Hewett, P. C., Foltz, C. B., Chaffee, F. H., Weymann, R. J., & Morris, S. L. 1991, ApJ, 373, 465
 Francis, P. J., Hooper, E. J., & Impey, C. D. 1993, AJ, 106, 417
 Green, P. J. 1998, ApJ, 498, 170
 Green, P. J. et al. 1995, ApJ, 450, 51
 Haardt, F. & Madau, P. 1996, ApJ, 461, 20
 Haehnelt, M. G., Madau, P., Kudritzki, R., & Haardt, F. 2001, ApJ, 549, L151
 Hamann, F., Cohen, R. D., Shields, J. C., Burbidge, E. M., Junkkarinen, V., & Crenshaw, D. M. 1998, ApJ, 496, 761
 Hamann, F., Zuo, L., & Tytler, D. 1995, ApJ, 444, L69
 Hu, E. M., Kim, T., Cowie, L. L., Songaila, A., & Rauch, M. 1995, AJ, 110, 1526

Impey, C. D., Petry, C. E., Malkan, M. A., & Webb, W. 1996, *ApJ*, 463, 473

Jakobsen, P., Boksenberg, A., Deharveng, J. M., Greenfield, P., Jedrzejewski, R., & Paresce, F. 1994, *Nature*, 370, 35

Kim, T., Hu, E. M., Cowie, L. L., & Songaila, A. 1997, *AJ*, 114, 1

Korista, K., Ferland, G., & Baldwin, J. 1997, *ApJ*, 487, 555

Kriss, G. 1994, in *ASP Conf. Ser. 61: Astronomical Data Analysis Software and Systems III*, Vol. 3, 437

Kriss, G. A. & Canizares, C. R. 1985, *ApJ*, 297, 177

Kriss, G. A. et al. 2001, *Science*, 293, 1112

Laor, A., Bahcall, J. N., Jannuzzi, B. T., Schneider, D. P., & Green, R. F. 1995, *ApJS*, 99, 1

Laor, A., Bahcall, J. N., Jannuzzi, B. T., Schneider, D. P., Green, R. F., & Hartig, G. F. 1994, *ApJ*, 420, 110

Laor, A., Fiore, F., Elvis, M., Wilkes, B. J., & McDowell, J. C. 1997a, *ApJ*, 477, 93

Laor, A., Jannuzzi, B. T., Green, R. F., & Boroson, T. A. 1997b, *ApJ*, 489, 656

Madau, P., Haardt, F., & Rees, M. J. 1999, *ApJ*, 514, 648

Madau, P. & Shull, J. M. 1996, *ApJ*, 457, 551

Marziani, P., Sulentic, J. W., Dultzin-Hacyan, D., Calvani, M., & Moles, M. 1996, *ApJS*, 104, 37

Mathews, W. G. & Ferland, G. J. 1987, *ApJ*, 323, 456

Mattig, W. 1958, *Astronomische Nachrichten*, 284, 109

Møller, P. & Jakobsen, P. 1990, *A&A*, 228, 299

Petitjean, P., Webb, J. K., Rauch, M., Carswell, R. F., & Lanzetta, K. 1993, *MNRAS*, 262, 499

Press, W. H., Rybicki, G. B., & Schneider, D. P. 1993, *ApJ*, 414, 64

Reimers, D., Köhler, S., Wisotzki, L., Groote, D., Rodriguez-Pascual, P., & Wamsteker, W. 1997, *A&A*, 327, 890

Sargent, W. L. W., Steidel, C. C., & Boksenberg, A. 1988, *ApJS*, 68, 539

Schlegel, D. J., Finkbeiner, D. P., & Davis, M. 1998, *ApJ*, 500, 525

Sramek, R. A. & Weedman, D. W. 1980, *ApJ*, 238, 435

Sulentic, J. W., Zwitter, T., Marziani, P., & Dultzin-Hacyan, D. 2000, *ApJ*, 536, L5

Tripp, T. M., Bechtold, J., & Green, R. F. 1994, *ApJ*, 433, 533

Tyler, D. 1987, *ApJ*, 321, 49

Vanden Berk, D. E. et al. 2001, *AJ*, 122, 549

Verner, E. M., Verner, D. A., Korista, K. T., Ferguson, J. W., Hamann, F., & Ferland, G. J. 1999, *ApJS*, 120, 101

Vogel, S. & Reimers, D. 1995, *A&A*, 294, 377

Wills, B. J., Brotherton, M. S., Fang, D., Steidel, C. C., & Sargent, W. L. W. 1993, *ApJ*, 415, 563

Yuan, W., Brinkmann, W., Siebert, J., & Voges, W. 1998, *A&A*, 330, 108

Zheng, W., Kriss, G. A., Telfer, R. C., Grimes, J. P., & Davidsen, A. F. 1997, *ApJ*, 475, 469 (Z97)

Zheng, W. et al. 2001, *ApJ*, submitted

Zuo, L. & Lu, L. 1993, *ApJ*, 418, 601